Visualizing electron beam-capping ligand reactions for controlled nanoparticle imaging with liquid phase transmission electron microscopy

*Thilini U. Dissanayake, Mei Wang, Taylor J. Woehl**

Department of Chemical and Biomolecular Engineering, University of Maryland, College Park, College Park, MD, USA 20742

Abstract

Liquid phase transmission electron microscopy (LP-TEM) enables real-time imaging of nanoparticle self-assembly, formation, and etching with single nanometer resolution. Despite the importance of organic nanoparticle capping ligands in these processes, the effect of electron beam irradiation on surface bound and soluble capping ligands during LP-TEM imaging has not been investigated. Here we use correlative LP-TEM and fluorescence microscopy (FM) to demonstrate that polymeric nanoparticle ligands undergo competing crosslinking and chain scission reactions that non-monotonically modify ligand coverage over time. Branched polyethylenimine (BPEI) coated silver nanoparticles were imaged with dose-controlled LP-TEM followed by labeling their primary amine groups with fluorophores to visualize the local thickness of adsorbed capping ligands. FM images showed that free ligands crosslinked in the LP-TEM image area over imaging times of tens of seconds, enhancing local capping ligand coverage on nanoparticles and silicon nitride membranes. Nanoparticle surface ligands underwent chain scission over irradiation times of minutes to tens of minutes, which depleted surface ligands from the nanoparticle and silicon nitride surface. Conversely, solutions of only soluble capping ligand underwent successive crosslinking reactions with no chain scission, suggesting nanoparticles enhanced the chain scission reactions by acting as radiolysis hotspots. The addition of a hydroxyl radical scavenger, tert-butanol, eliminated chain scission reactions and slowed the progression of crosslinking reactions. These experiments have important implications for performing controlled and reproducible LP-TEM nanoparticle imaging as they demonstrate the electron beam can significantly alter ligand coverage on nanoparticles in a non-intuitive manner. They emphasize the need to understand and control the electron beam radiation chemistry of a given sample to avoid significant perturbations to the nanoparticle capping ligand chemistry, which are invisible in electron micrographs.

Introduction

Self-assembly of colloidal nanoparticles enables constructing intricate nanostructures and macroscopic materials that cannot be realized by top-down processing.[1-2] Self-assembly of nanoparticles is a complex process in which both thermodynamics and kinetics play important and intertwined roles in determining the final self-assembled structure.[3] Liquid phase transmission electron microscopy (LP-TEM) can uniquely visualize the dynamics of nanoparticle self-assembly in a liquid medium in real time with nanometer scale resolution. Numerous LP-TEM studies have investigated self-assembly of nanoparticles functionalized with small molecules, polymers, and DNA capping ligands.[4-24] Interparticle interactions during self-assembly, including steric forces, electrostatic forces, hydrogen bonding, and hydrophobic/hydrophilic forces are mediated by the specific physicochemical properties (*e.g.* molecular weight, ligand density, functional groups, protonation/deprotonation) of organic surface ligands on nanoparticles.[1, 25] It is well known that the TEM beam strongly interacts with organic molecules through radiolysis reactions.[26-27] However, despite the importance of organic capping ligands in self-assembly and their susceptibility to electron beam damage,[28] few LP-TEM studies have focused on electron beam damage mechanisms of organic capping ligands. To correctly interpret self-assembly dynamics and mechanisms observed with LP-TEM, it is imperative to understand how the electron beam modifies nanoparticle surface ligands and to establish limits on the electron doses and dose rates used to image nanoparticle self-assembly.

The electron beam creates highly reactive radicals through solvent radiolysis during LP-TEM imaging. For instance, radiolysis of water creates both strongly reducing radicals, aqueous electrons (e_{aq}^-) and hydrogen radicals ($H^{\cdot}$), and oxidizing hydroxyl radicals ($OH^{\cdot}$), which can react with organic molecules.[27, 29] While electron beam-sample interactions have been extensively studied in terms of general radiolysis reactions and formation of metal nanocrystals, [9, 30] little work has been performed to understand how these radical reactions impact organic capping ligands. The radiation chemistry field has shown that

radicals readily react with organic molecules and polymer through various redox processes.[31-40] Given the large number of LP-TEM studies on self-assembly, the lack of systematic studies of electron beam reactions with nanoparticle surface ligands has prohibited discovery of acceptable "low dose" imaging conditions for LP-TEM nanoparticle self-assembly experiments that produce minimal beam induced changes to nanoparticle surface chemistry.

Electron beam induced reactions during LP-TEM are only perceptible if visible changes occur in the material being imaging, *e.g.*, growth/etching of nanoparticles,[41-46] dissolution of metal organic frameworks,[47] pitting of carbon nanotubes,[48] shrinkage of bacterial cells,[49] or formation of visible polymeric nanoparticles.[50] Nanoparticle surface ligands are not observed during LP-TEM due to their small size (typically < 2 nm ligand layer thickness) and low image contrast compared to inorganic nanoparticles. Even if ligands can be visualized with state-of-the-art aberration corrected or graphene liquid cell TEM, LP-TEM images provide no information about the chemical structure of the ligands. In this article, we employ fluorescent probes and correlative fluorescence microscopy (FM) to establish the fate of excess and adsorbed capping ligands during LP-TEM imaging. Our results show that polymer crosslinking and chain scission occur during LP-TEM imaging, leading in some cases to a non-monotonic time dependent change in ligand thickness on the nanoparticles and the silicon nitride membrane surface. The results emphasize the magnifying effect of high atomic number nanoparticles on local radiation damage, in agreement with a recent report,[50] and the effectiveness of radical scavengers in mitigating electron beam damage. We expect this method can be applied to other nanoparticle surface ligands as well as biomolecules by drawing from the extensive library of conjugation reactions developed for conjugating fluorophores to biomolecules.

Methods

Preparation of nanoparticles and LP-TEM samples

An aqueous suspension of 100 nm BPEI coated silver nanoparticles was purchased from nanoComposix (San Diego, USA). BPEI covalently bonds to the surface of silver nanoparticles *via* amine-metal binding with an approximate grafting density of 0.05 molecules/nm^2 (calculated based on a ~1 nm ligand shell thickness observed in TEM images). The silver nanoparticles were centrifuged and washed with DI water two times to remove excess ligands and contaminants. Liquid cell silicon nitride chips (Protochips) with 500 µm × 50 µm silicon nitride windows and 500 nm gold spacers were rinsed consecutively with acetone and methanol and were treated with an air plasma for 2 minutes to render them hydrophilic and remove residual organics. Three 5 µl drops of silver nanoparticles were consecutively air dried on the silicon nitride windows of both top and bottom chips **(Figure 1**, step 1). The membranes were rinsed with DI water after nanoparticle deposition. For experiments using only BPEI ligands, the twice cleaned nanoparticle solution was centrifuged a third time and three 5 µl drops of clear supernatant were air dried on the silicon nitride membranes. The silicon chips were assembled dry in the liquid cell holder (Protochips) and HPLC grade water was flowed into the cell using a syringe pump (Harvard Apparatus) at a rate of 300 µl/h **(Figure 1** step 2). For experiments with radical scavenger, 1 M tert-butanol in HPLC grade water was flowed into the cell.

LP-TEM experiments

LP-TEM imaging was performed in a JEOL JEM-2100F field emission electron microscope operating at 200 kV in STEM mode at a magnification of 20,000x. After focusing and rotating the beam to align with the edge of the silicon nitride membrane, the sample was translated to one corner of the silicon nitride membrane. Different regions of the silicon nitride membrane were irradiated at electron fluxes ranging from 0.032 - 0.138 $e^-/Å^2$ s (dose rate of 0.144 – 0.616 MGy/s) for 30 s - 10 min **(Figure 1**, step 3). The spaces between each irradiated area were systematically varied to create an easily identifiable pattern in the FM image to correlate each irradiated area with the respective exposure time and dose. Other than to demonstrate how the electron beam reacts with ligands while translating, rotating, or focusing the

sample, the electron beam was blanked when moving to a new region using an electrostatic blanker. LP-TEM images showed nanoparticles were deposited onto the membrane surface as single particles and aggregates (**Figure 1**, top right). The liquid cell was disassembled carefully after the LP-TEM experiment and silicon chips were removed from the holder with the silicon nitride windows intact (**Figure 1** step 4).

Fluorescence labeling of samples and fluorescence microscopy

A 10 mg/ml stock solution of fluorophore was prepared by dissolving 2 mg of 6-[Fluorescein-5(6)-carboxamido]hexanoic acid (Sigma) in 200 µl of dimethyl sulfoxide (DMSO). 25 µl of 16 mg/ml 1-Ethyl-3-(3-dimethylaminopropyl)carbodiimide (EDC, Thermo Scientific), and 25 µl of 44 mg/ml N-hydroxysulfosuccinimide (Sulfo-NHS, Thermo Scientific) were added to 100 µl of the fluorophore stock solution and left to react for 15 minutes at room temperature to form an amine reactive fluorophore. After that, 0.28 µl of 2-Mercaptoethanol (Thermo Scientific) was added to the fluorescein – EDC – NHS solution and incubated for 5 minutes to quench excess EDC in the solution. The disassembled top and bottom liquid cell chips were placed in 425 µl of DI water in a centrifuge tube and 75 µl of fluorescein – EDC – NHS solution was injected. The reaction between the amine reactive fluorophore and primary amine groups on the BPEI molecules proceeded for 1 hour after which the chips were washed 3 times with DI water **(Figure 1**, step 5). The cleaned chips were dried using compressed air and placed on a clean cover slip. FM was performed in an inverted optical microscope (ZEISS Axio Observer) with a 40x dry objective lens **(Figure 1**, step 6). All the FM images in this study originated from the top chip of the liquid cell in each experiment because this is where the electron beam was focused during LP-TEM. FM images were processed and analyzed using ImageJ.[51] Silicon nitride membrane fluorescence intensity profiles were measured along lines draw across the image area with each intensity divided by the background fluorescence intensity immediately outside the image area. Fluorescence intensities of nanoparticles were determined by measuring the average intensity of each nanoparticle.

We labeled the BPEI capping ligands after the sample was imaged and removed from the TEM to avoid electron beam damage to fluorescent molecules, which can extinguish their fluorescence emission. The FM images provided a snapshot of the local relative BPEI ligand thickness for a given LP-TEM imaging time and cumulative dose. Benchtop control experiments varying the thickness of polymer layers on flat silicon substrates were performed to validate the method. A solution of fluorescein labeled BPEI was serially diluted to various polymer concentrations and dried on silicon chips to create samples with linearly varying BPEI thicknesses. FM images were taken of each sample and average fluorescence intensity measurements were linearly proportional to the BPEI solution concentration (**Figure S1**), and thus linearly proportional to the local thickness of BPEI on the surface.

Results

Systematic dose rate-controlled LP-TEM experiments probing electron beam reactions with nanoparticle capping ligands were performed on 100 nm diameter silver nanoparticles coated with 25,000 g/mol BPEI, which contains primary, secondary, and tertiary amine groups that imbue the nanoparticle surfaces with a positive charge (**Figure 2a**). TEM images of the silver nanoparticles in the dry state showed they were either spherical or faceted, polycrystalline, had a monomodal size distribution (**Figure 2 b,c**), and were coated by a ~1 nm thick BPEI ligand layer (**Figure 2d**). Due to the low spatial resolution of the FM images (~500 nm), low magnification (M = 20,000 x) scanning TEM mode (STEM) was used for all LP-TEM experiments to create a large irradiated region on the order of 10 μm that could be visualized with FM. Within each irradiated area, each nanoparticle or nanoparticle aggregate was exposed to a uniform dose rate and cumulative electron dose. In this article, we report the dose rate in units of Grays per second (Gy/s), which is the product of the area averaged electron flux (electron beam current divided by the image area size) and stopping power of water (2.798×10^5 eV.m^2/kg), following previously established methods.[9, 43] Cumulative doses given in each figure were calculated by multiplying the dose

rate by the total irradiation time. We note that electron fluxes (0.032 - 0.138 $e^-/Å^2s$) and cumulative electrons delivered (1 – 80 $e^-/Å^2$) used here are generally considered to be "low dose" conditions used for imaging electron beam sensitive polymers and biomolecules with LP-TEM and cryo-EM.[52-55]

FM images showed background fluorescence across the silicon nitride surface from adsorbed BPEI ligands, while silver nanoparticles and nanoparticle aggregates appeared as bright fluorescent spots above the background (**Figure 3a**). Some sample regions had bright fluorescence and nanoparticle coverage due to evaporation induced aggregation of nanoparticles (left side of **Figure 3a**); these regions were not considered in quantitative analyses. Sample regions irradiated by the electron beam were clearly distinguished as bright or dark square regions with sizes roughly equal to the STEM image size. Two characteristic features were immediately evident in the FM images (**Figure 3a**). The first feature was squares or tracks across the membrane surface that were brighter than the background; these regions corresponded to image regions irradiated with the electron beam for < 30 s during focusing, sample translation (**Figure 3b**), or image rotation (**Figure 3c**). We did not know the exact irradiation time for these as the shortest timed irradiation was 5 minutes, but these image manipulations typically took ≤ 30 s. Nanoparticles in these regions had brighter fluorescence intensity than non-irradiated nanoparticles. The second type of fluorescent feature observed was image areas that were similar intensity or darker than the background intensity and surrounded by a bright fluorescent halo and corresponded to image regions irradiated for > 5 minutes (**Figure 3d**). Nanoparticles within these dark regions had lower fluorescence intensity compared to those in the bright irradiated regions and unirradiated regions. In most cases, nanoparticles remained immobile on the silicon nitride membranes throughout the irradiation experiments and no beam induced nanoparticle aggregation was observed (**Supplementary movie 1**). At a relatively high dose rate of 0.616 MGy/s, some nanoparticles moved into the image area in the first few seconds after which they were immobile for the rest of the irradiation, indicating they received a nearly identical cumulative dose compared to the initially present particles (**Figure S2**).

Systematic irradiation experiments and quantitative fluorescence intensity measurements revealed how the total dose impacted the local surface thickness of BPEI ligands on the silicon nitride membrane for samples with and without nanoparticles present (**Figure 4**). Image areas irradiated for times of 5 and 10 minutes at a dose rate of 0.324 MGy/s during LP-TEM resulted in cumulative doses corresponding to 97.1 MGy and 194.1 MGy while regions irradiated for < 30 seconds received cumulative doses of < 9.7 MGy. All regions irradiated for < 30 seconds were brighter than the non-irradiated surrounding area (**Figure 4a**), while those irradiated for > 5 minutes were either lower intensity or similar intensity compared to the background (**Figure 4b,c**). For the longer irradiation times, the intensity inside the irradiated regions and the intensity of the surrounding fluorescent halo showed no trend with cumulative dose (**Figure 4d**). We did not observe any effect of the dose rate on the qualitative effects of LP-TEM irradiation, as irradiating a sample at a dose rate of 0.616 MGy/s yielded a similar sequence of events as the lower dose rate (**Figure S3**). To test the effect of nanoparticles on the electron beam damage to the ligands, we irradiated a separate sample containing only excess soluble BPEI capping ligand. The sample regions exposed to the electron beam for 1 minute were barely discernible (**Figures 4e**). In contrast to the experiments with nanoparticles present, bright fluorescence intensity was observed in image regions irradiated for 5 (82 MGy) and 10 minutes (164 MGy) (**Figures 4e-g**). The fluorescence intensity of the silicon nitride increased by ~10% between the 5 minute and 10 minute irradiations (**Figures 4h**).

In addition to changing the fluorescence intensity of the membrane surface, irradiation during LP-TEM modified the fluorescence intensity, and thus the ligand coverage, of silver nanoparticles compared to non-irradiated areas. Nanoparticles displayed a distribution of fluorescence intensities due to variations in initial ligand coverage, particle size, and particle aggregation, so we performed a statistical analysis of the effect of cumulative dose on nanoparticle fluorescence intensity (**Figure 5**). Measurements of nanoparticles intensities were merged for all < 30 sec irradiation areas and all > 5 min irradiation areas shown in **Figure 3a** to gain statistically significant population sizes (> 40 particles per data set).

Histograms of individual particle fluorescence intensities showed the nanoparticle intensity distribution for regions irradiated for > 5 minutes was lower overall compared to unirradiated regions, while nanoparticles irradiated for < 30 seconds had overall larger fluorescence intensities (**Figure 5a**). A statistical comparison of intensity distributions revealed that each intensity distribution was statistically different (for $P < 0.005$) (**Figure 5b**). The changes in the nanoparticle fluorescence intensities with cumulative dose therefore mirrored those of the silicon nitride membranes, indicating that similar chemical processes controlled ligand damage on the silicon nitride and silver nanoparticles.

Prior works have established that alcohols, such as isopropanol and tert-butanol, and other organic molecules can act as hydroxyl radical scavengers to mitigate radiation damage to organic molecules during LP-TEM imaging.[50, 56-59] We added 1 M tert-butanol in DI water as a radical scavenger to test its impact on electron beam damage of BPEI in the presence of silver nanoparticles (**Figure 6**). Similar to the experiment without any nanoparticles, there was no visible change in fluorescence intensity in the image regions exposed for 30 seconds and 1 minute at a dose rate of 0.274 MGy/s. Compared to samples with no tert-butanol irradiated for > 5 min, which showed decreased fluorescence intensity, a small increase in fluorescence intensity compared to background was observed at similar irradiation times for the nanoparticle sample containing tert-butanol (**Figure 6a-c**). The largest fluorescence intensity of the sample region irradiated with tert-butanol present (≈ 1.6) was smaller than the sample with no tert-butanol (≈ 2) after being irradiated with 10 times less cumulative dose.

Discussion

The electron beam indirectly reacts with soluble and nanoparticle surface adsorbed polymers in aqueous solution *via* radicals formed by water radiolysis, including oxidizing hydroxyl radicals ($OH^{\cdot}$), reducing hydrogen radicals ($H^{\cdot}$), and reducing aqueous electrons (e^{-}_{aq}).[27, 38, 60] Hydroxyl radicals readily react with polymers by abstracting hydrogen atoms from the main carbon chain and amine groups, which

forms reactive radicals that either undergo intramolecular or intermolecular crosslinking or serve as intermediates to carbon-carbon chain scission reactions.[61] Radiation induced crosslinking reactions have been utilized to form hydrogels and bulk polymers by irradiating both solid phase and liquid phase precursors.[38, 61-63] While each of the three reactions occur simultaneously, the dominant reaction is influenced by polymer chemistry, molecular weight, concentration, dose rate, and cumulative dose. The fluorescence labeling approach used in this study distinguishes between intermolecular crosslinking (enhanced local fluorescence intensity with electron irradiation) and chain scission (reduced local fluorescence intensity with electron irradiation), but cannot readily identify intramolecular crosslinking, which will change the local ligand layer thickness but not the fluorescence intensity. However, because the polymer used here is 25,000 g/mol, which is a relatively low molecular weight, we expect intermolecular crosslinking to dominate over intramolecular crosslinking.[40] Based on these reactions, we interpreted irradiated regions that were darker compared to the background as those where chain scission reactions dominated for the given cumulative dose, while brighter fluorescent regions experienced net intermolecular crosslinking.

In addition to radical reactions, we also considered the effect of electric fields on the deposition/removal of BPEI ligands from the image area. It is well known that the thin solid silicon nitride membranes emit secondary electrons during LP-TEM imaging, which can induce a positive charge on the membrane.[64] Positive charge on the silicon nitride gives rise to a divergent electric field inside the liquid directed away from the irradiated region of the membrane into the bulk liquid.[65] If this field is sufficiently strong, it could impact the attachment of BPEI to the negatively charged silicon nitride membrane as well as the transport of the positively charged polymer in solution. Recent studies have provided conflicting estimates of the local electric field and membrane potential during LP-TEM. The electron beam induced membrane potential was estimated to be +2 mV by prior Monte-Carlo scattering simulations.[30] The silicon nitride-water interface has a zeta potential of about -30 mV near neutral pH, so this beam induced surface

potential would not significantly affect the overall membrane surface potential. Another recent study concluded that there will be no appreciable electric field in the system due to charge screening at the solid-liquid interface.[66] However, several other studies suggested more significant electric fields form due to beam induced charging, but did not offer any practical estimates of their magnitudes in the presence of liquid.[65, 67] The observation that the solution chemistry and cumulative dose, and not the dose rate (which controls the magnitude of electron beam charging[67]), controlled whether ligand was added or removed from the irradiated area suggests that radiation chemistry mediates the observed phenomena and not beam induced charging. However, due to the lack of comprehensive studies on electric fields during LP-TEM we cannot completely disregard electric fields and acknowledge that they could affect polymer transport in solution and local radical concentrations.

Positively charged nanoparticles and free BPEI ligand initially dried onto the negatively charged silicon nitride surface physisorbed by electrostatic interactions. Any loosely bound or entangled nanoparticles and polymers on top of this adsorbed layer become solubilized after water was introduced into the liquid cell. The adsorbed and soluble BPEI ligands reacted with radicals created by the electron beam and crosslinking and chain scission reactions proliferated. In DI water only, the fluorescence intensity of the silicon nitride membrane and nanoparticles locally increased after short irradiation times (~30 seconds) due to crosslinking of soluble BPEI to BPEI adsorbed to nanoparticles and the silicon nitride membrane. Previous work has shown that radical concentrations are elevated near the water – silicon nitride interface and near nanoparticle surfaces,[68] which enhances local production of BPEI radicals compared to bulk solution. The initial rate of BPEI crosslinking reactions was higher than the rate of chain scission as evidenced by the increased fluorescence intensity. Over several minutes, soluble BPEI ligands were depleted by the crosslinking reactions and the hydrogen abstraction rate constant, which creates crosslinking sites, decreased due to the increasing BPEI molecular weight.[37] Moreover, electrostatic repulsion between similarly charged BPEI molecules could play a role in slowing the crosslinking reaction

rate over time.[39] Due to the increase in the radical lifetime on BPEI molecules, resulting from the decreased free BPEI concentration and crosslinking reaction rates, chain scission reactions began to dominate over crosslinking, leading to decreased fluorescence intensity in the image regions irradiated for several minutes. While this method does not detect intramolecular crosslinking, it is possible the BPEI ligands crosslinked onto the surface underwent intramolecular crosslinking as alkyl radicals continued to form in close proximity. During the chain scission process, rupture of the bonds between BPEI and silver surface is not expected to be a significant reaction due to the abundance of reactive C – H and N – H bonds in BPEI polymers. We do not expect reactions between radicals and the polymer-nanoparticle or polymer-silicon nitride bonds to be significant due to their low abundance compared to the PEI repeat units. BPEI fragments from chain scission reactions did not crosslink again inside the image area but transported away and crosslinked outside the image area as apparent by bright halos surrounding the irradiated regions. In the absence of nanoparticles and when 1 M tert-butanol was included with the nanoparticles, BPEI ligands only displayed net crosslinking reactions across all doses and dose rates tested.

Recent studies showing amplification of electron beam damage and radical concentrations by high atomic number nanoparticles provide clues about the different behaviors of the nanoparticle laden, nanoparticle free, and radical scavenger laden samples. Korpanty *et al.* found that gold nanoparticles accelerated the radiation crosslinking of polyethylene glycol and found through modeling that nanoparticles enhanced the yields of hydroxyl and polymer radicals.[50] Prior numerical radiolysis simulations predicted that the local yield of radicals was several times higher near a metal – water interface compared to bulk liquid due higher yield of secondary and backscattered electrons from metals when irradiated.[68] In the field of radiation processing of bulk polymers, empirical evidence shows that crosslinking predominates at low cumulative dose while chain scission dominates at larger cumulative doses. This occurs because the yields for crosslinking and chain scission increase as a function of cumulative dose and the chain scission yield increases more rapidly.[62] Finally, prior simulations by Wang

et al. found that addition of tert-butanol reduced the steady state hydroxyl radical concentration in water by several orders of magnitude.[56] Taken together, these prior studies suggest that silver nanoparticles created larger concentrations of hydroxyl radicals, which accelerated the electron beam damage process of crosslinking at low cumulative dose followed by chain scission at high cumulative dose. In the absence of nanoparticles or in the presence of tert-butanol, the hydroxyl radical concentration decreased and crosslinking was the dominant reaction over the experimental time scales. In other words, the effective cumulative dose was higher with nanoparticles present and was lower in the absence of nanoparticles and with tert-butanol present. These results demonstrate that chain scission reactions, which will deplete the ligand shell and negatively affect the nanoparticle stability and potential to undergo self-assembly, could be avoided by using a radical scavenger or reducing nanoparticle concentration.

An overall picture of the dominant radical reactions as a function of cumulative dose for nanoparticles in DI water, soluble BPEI in DI water, and nanoparticles with radical scavenger is illustrated in **Figure 7**. The colors in each horizontal bar denote the approximate range of cumulative doses where each radical reaction dominated for each type of sample, as observed by FM, with white corresponding to no perceivable change to the sample. As metallic nanoparticles enhanced electron beam damage to ligands near the surface, removing much of the excess ligand prior to experiments can prevent the initial crosslinking reactions. Our experiments demonstrated that electron beam alterations to surface capping ligands could be delayed to some extent by including a radical scavenger. The time dependent ligand surface coverage on nanoparticles and the silicon nitride membrane during LP-TEM experiments has several implications for the colloidal and interfacial properties of LP-TEM nanoparticle samples. First, removal or addition of ligands by radical reactions modifies the surface charge on the nanoparticles and silicon nitride membranes. While fluorescence intensity changes do not directly correspond to changes in surface charge, there is clearly a significant change in ligand surface coverage on nanoparticles after electron beam irradiation, especially at short times in the absence of radical scavengers. The radiation

induced reactions can have significant effects on the surface charge of nanoparticles and thus on their electrostatic and steric colloidal interactions and overall colloidal stability. Changes in surface charge and ligand coating thickness will impact nanoparticle-nanoparticle and nanoparticle-membrane interactions during self-assembly. Perhaps the most interesting observation is that the most significant changes in surface concentration of ligands occurred at *short times and for low cumulative doses*, indicating low dose imaging alone may not be effective at preventing significant electron beam modifications to polymer capping ligands and that radical scavengers must be used in concert with low dose imaging.

Several prior works by our group and others have demonstrated irreversible electron beam induced aggregation of polymer ligand capped nanoparticles during LP-TEM.[4, 57, 64] It is plausible that electron beam induced intermolecular crosslinking and chain scission of polymer ligands will contribute to nanoparticle aggregation by reducing nanoparticle colloidal stability or covalently linking nanoparticles together. An important implication of this process is that irreversible electron beam induced aggregation of nanoparticles is a kinetically controlled process driven by radical reactions, making it distinct from self-assembly, which is a reversible process driven by interparticle interactions. Even though radiation induced crosslinking can explain some nanoparticle systems with high molecular weight polymeric ligands, it appears that nanoparticles capped with small molecules do not display irreversible nanoparticle aggregation. For an example, recent LP-TEM self-assembly studies of nanoparticles capped with small molecules (*e.g.*, carboxylic acids, cationic surfactants) showed reversible assembly under electron beam irradiation, implying that electron beam damage to the surface ligand coating did not result in irreversible aggregation.[14, 21] Prior LP-TEM experiments have shown that BPEI functionalized nanoparticles attached to the silicon nitride membrane began to diffuse under electron irradiation after an initial lag time.[69] Prior studies have posited this was due to radiation induced changes in pH[70] or electron beam charging of the silicon nitride membranes,[69] but pH changes and charging occur on short time scales (milliseconds) compared to the lag time for particle motion to begin (tens of seconds).[29] Our results show that ligand

surface concentrations can increase on the nanoparticles and silicon nitride membranes over tens of seconds, which could increase repulsive steric and electrostatic forces.

The specific functional groups present on a polymer ligand will mediate the type of radiation reactions it undergoes upon electron beam irradiation. Aqueous PEI solutions degrade upon electron irradiation by chain scission reactions at secondary amine sites and carbon-carbon bonds in the main polymer chain.[31] At neutral pH values, primary amine groups on PEI are mostly protonated and repulsive electrostatic forces between positively charged polymer molecules may prevent crosslinking. Similar effects are observed for polyacrylic acids where negatively charged carboxyl groups suppress crosslinking reactions; crosslinking was only observed at acidic pH values (~2) where most carboxylic acids were uncharged.[39] Similarly, polymethacrylic acids prefer chain scission over crosslinking and degrade by β-fragmentation of alkyl radicals formed during radiolysis.[71] Chitosan, a polymer molecule containing amine and hydroxyl functional groups predominantly undergoes chain scission through peroxyl radicals formed in the presence of oxygen or through scission of glycosidic bonds in deoxygenated solutions.[72] A recent study by our group showed that PEG – SH ligands act as radical scavengers for hydroxyl radicals by hydrogen abstraction from the thiol groups and PEG chain.[57] In aqueous solutions of PEG and polyacrylamide, an uncharged polymer, intermolecular and intramolecular crosslinking prevails over degradation in deoxygenated solutions while main chain scission dominates with oxygen present.[40, 73,74] Therefore, the molecular structure of the ligands are important in determining the successive radiation driven reactions of polymeric capping ligands during LP-TEM experiments.

Conclusion

We utilized correlative LP-TEM and FM to investigate electron beam modification of BPEI capping ligands for controlled nanoparticle imaging with LP-TEM. BPEI coated silver nanoparticles irradiated in LP-TEM for different times and cumulative doses were labeled with fluorescent molecules

after imaging, which enabled directly visualizing the outcome of electron beam driven reactions with capping ligands. Two competing electron beam induced reactions, intermolecular crosslinking and chain scission, determined the fluorescence intensity of the nanoparticles and silicon nitride membrane with irradiation time. Crosslinking reactions dominated at short irradiation times due to high concentrations of free BPEI ligand in solution and high crosslinking reaction rate constant, while chain scission reactions dominated for irradiation times of > 5 minutes due to increased concentration of crosslinked polymers and decreased soluble polymer concentration. Crosslinking dominated for all cumulative doses tested in the absence of nanoparticles and for nanoparticles in the presence of tert-butanol as a radical scavenger. The observations are explained in terms of kinetic competition between crosslinking and chain scission reactions and the relative amounts of oxidizing hydroxyl radicals created. Competing electron beam reactions are expected to modify the surface properties and colloidal interactions of the nanoparticles and silicon nitride membranes by modifying electrostatic and steric interparticle interactions. This method can be extended to probe other capping ligand chemistries, such as carboxylic acid or thiol moieties, by utilizing commercially available fluorophore conjugation chemistries developed for biomolecules. We expect the specific response of a capping ligand to the electron beam will be chemistry and solvent specific. The example of BPEI ligand reactions serves as an initial demonstration of how correlative FM and LP-TEM to track electron beam-ligand reactions and demonstrates the potentially complex and time dependent modifications the electron beam can induce in the surface ligand chemistry and concentration, even for low dose imaging conditions.

Associated content

Supporting Information

Supporting movie file; Control experiments showing fluorescence intensity changes with BPEI concentration/thickness; Nanoparticle mobility during LP-TEM; Effect of LP-TEM imaging time and cumulative dose on the fluorescence intensity of the labeled silicon nitride membrane at additional dose rates.

AUTHOR INFORMATION

Corresponding Author

Taylor J. Woehl – Department of Chemical and Bimolecular Engineering, University of Maryland, College Park, College Park, MD 20742; https://orcid.org/0000-0002-4000-8280; Phone: 301-405-1074; Email: tjwoehl@umd.edu

Authors

Thilini Umesha Dissanayake – Department of Chemical and Bimolecular Engineering, University of Maryland, College Park, College Park, MD 20742

Mei Wang – Department of Chemical and Bimolecular Engineering, University of Maryland, College Park, College Park, MD 20742

Notes

The authors declare no competing financial interests.

ACKNOWLEDGEMENTS

T.J.W. and T.U.D. acknowledge funding from the Army Research Office (Award #W911NF2010169).

We acknowledge Sz-Chian Liu in the University of Maryland AIMlab for assistance in TEM operation.

We thank J. Patterson and W. Gibson for useful discussions on electron beam polymerization.

References

(1) Boles, M. A.; Engel, M.; Talapin, D. V. Self-Assembly of Colloidal Nanocrystals: From Intricate Structures to Functional Materials. *Chemical reviews* **2016,** *116* (18), 11220-89, DOI: 10.1021/acs.chemrev.6b00196.
(2) Cademartiri, L.; Bishop, K. J. Programmable self-assembly. *Nature materials* **2015,** *14* (1), 2-9, DOI: 10.1038/nmat4184.
(3) Whitelam, S.; Jack, R. L. The statistical mechanics of dynamic pathways to self-assembly. *Annual review of physical chemistry* **2015,** *66*, 143-63, DOI: 10.1146/annurev-physchem-040214-121215.
(4) Cepeda-Perez, E.; de Jonge, N. Dynamics of gold nanoparticle clusters observed with liquid-phase electron microscopy. *Micron* **2019,** *117*, 68-75, DOI: 10.1016/j.micron.2018.11.006.

(5) Cepeda-Perez, E.; Doblas, D.; Kraus, T.; de Jonge, N. Electron microscopy of nanoparticle superlattice formation at a solid-liquid interface in nonpolar liquids. *Science advances* **2020,** *6* (20), eaba1404.
(6) Jungjohann, K. L.; Wheeler, D. R.; Polsky, R.; Brozik, S. M.; Brozik, J. A.; Rudolph, A. R. Liquid-cell scanning transmission electron microscopy and fluorescence correlation spectroscopy of DNA-directed gold nanoparticle assemblies. *Micron* **2019,** *119*, 54-63, DOI: 10.1016/j.micron.2018.11.004.
(7) Keskin, S.; Besztejan, S.; Kassier, G. n.; Manz, S.; Bücker, R.; Riekeberg, S.; Trieu, H. K.; Rentmeister, A.; Miller, R. D. Visualization of multimerization and self-assembly of DNA-functionalized gold nanoparticles using in-liquid transmission electron microscopy. *The journal of physical chemistry letters* **2015,** *6* (22), 4487-4492.
(8) Kim, J.; Ou, Z.; Jones, M. R.; Song, X.; Chen, Q. Imaging the polymerization of multivalent nanoparticles in solution. *Nature communications* **2017,** *8* (1), 761, DOI: 10.1038/s41467-017-00857-1.
(9) Lee, J.; Nakouzi, E.; Song, M.; Wang, B.; Chun, J.; Li, D. Mechanistic Understanding of the Growth Kinetics and Dynamics of Nanoparticle Superlattices by Coupling Interparticle Forces from Real-Time Measurements. *ACS nano* **2018,** *12* (12), 12778-12787, DOI: 10.1021/acsnano.8b07880.
(10) Liu, C.; Ou, Z.; Guo, F.; Luo, B.; Chen, W.; Qi, L.; Chen, Q. "Colloid-Atom Duality" in the Assembly Dynamics of Concave Gold Nanoarrows. *Journal of the American Chemical Society* **2020,** *142* (27), 11669-11673, DOI: 10.1021/jacs.0c04444.
(11) Liu, Y.; Lin, X. M.; Sun, Y.; Rajh, T. In situ visualization of self-assembly of charged gold nanoparticles. *Journal of the American Chemical Society* **2013,** *135* (10), 3764-7, DOI: 10.1021/ja312620e.
(12) Luo, B.; Smith, J. W.; Ou, Z.; Chen, Q. Quantifying the self-assembly behavior of anisotropic nanoparticles using liquid-phase transmission electron microscopy. *Accounts of chemical research* **2017,** *50* (5), 1125-1133.
(13) Miele, E.; Raj, S.; Baraissov, Z.; Kral, P.; Mirsaidov, U. Dynamics of Templated Assembly of Nanoparticle Filaments within Nanochannels. *Advanced materials* **2017,** *29* (37), DOI: 10.1002/adma.201702682.
(14) Ou, Z.; Wang, Z.; Luo, B.; Luijten, E.; Chen, Q. Kinetic pathways of crystallization at the nanoscale. *Nature materials* **2020,** *19* (4), 450-455, DOI: 10.1038/s41563-019-0514-1.
(15) Park, J.; Zheng, H.; Lee, W. C.; Geissler, P. L.; Rabani, E.; Alivisatos, A. P. Direct observation of nanoparticle superlattice formation by using liquid cell transmission electron microscopy. *ACS nano* **2012,** *6* (3), 2078-85, DOI: 10.1021/nn203837m.
(16) Powers, A. S.; Liao, H. G.; Raja, S. N.; Bronstein, N. D.; Alivisatos, A. P.; Zheng, H. Tracking Nanoparticle Diffusion and Interaction during Self-Assembly in a Liquid Cell. *Nano letters* **2017,** *17* (1), 15-20, DOI: 10.1021/acs.nanolett.6b02972.
(17) Sutter, E.; Sutter, P.; Tkachenko, A. V.; Krahne, R.; de Graaf, J.; Arciniegas, M.; Manna, L. In situ microscopy of the self-assembly of branched nanocrystals in solution. *Nature communications* **2016,** *7*, 11213, DOI: 10.1038/ncomms11213.
(18) Sutter, E.; Zhang, B.; Sutter, S.; Sutter, P. In situ electron microscopy of the self-assembly of single-stranded DNA-functionalized Au nanoparticles in aqueous solution. *Nanoscale* **2018,** *11* (1), 34-44, DOI: 10.1039/c8nr08421a.
(19) Tan, S. F.; Anand, U.; Mirsaidov, U. Interactions and Attachment Pathways between Functionalized Gold Nanorods. *ACS nano* **2017,** *11* (2), 1633-1640, DOI: 10.1021/acsnano.6b07398.
(20) Tan, S. F.; Chee, S. W.; Lin, G.; Mirsaidov, U. Direct Observation of Interactions between Nanoparticles and Nanoparticle Self-Assembly in Solution. *Accounts of chemical research* **2017,** *50* (6), 1303-1312, DOI: 10.1021/acs.accounts.7b00063.
(21) Tan, S. F.; Raj, S.; Bisht, G.; Annadata, H. V.; Nijhuis, C. A.; Kral, P.; Mirsaidov, U. Nanoparticle Interactions Guided by Shape-Dependent Hydrophobic Forces. *Advanced materials* **2018,** *30* (16), e1707077, DOI: 10.1002/adma.201707077.
(22) Wang, Y.; Peng, X.; Abelson, A.; Xiao, P.; Qian, C.; Yu, L.; Ophus, C.; Ercius, P.; Wang, L. W.; Law, M.; Zheng, H. Dynamic deformability of individual PbSe nanocrystals during superlattice phase transitions. *Science advances* **2019,** *5* (6), eaaw5623, DOI: 10.1126/sciadv.aaw5623.
(23) Wang, Y.; Peng, X.; Abelson, A.; Zhang, B.-K.; Qian, C.; Ercius, P.; Wang, L.-W.; Law, M.; Zheng, H. In situ TEM observation of neck formation during oriented attachment of PbSe nanocrystals. *Nano Research* **2019,** *12* (10), 2549-2553.

(24) Zhu, C.; Liang, S.; Song, E.; Zhou, Y.; Wang, W.; Shan, F.; Shi, Y.; Hao, C.; Yin, K.; Zhang, T.; Liu, J.; Zheng, H.; Sun, L. In-situ liquid cell transmission electron microscopy investigation on oriented attachment of gold nanoparticles. *Nature communications* **2018,** *9* (1), 421, DOI: 10.1038/s41467-018-02925-6.
(25) Bishop, K. J.; Wilmer, C. E.; Soh, S.; Grzybowski, B. A. Nanoscale forces and their uses in self-assembly. *Small* **2009,** *5* (14), 1600-30, DOI: 10.1002/smll.200900358.
(26) Cookman, J.; Hamilton, V.; Price, L. S.; Hall, S. R.; Bangert, U. Visualising early-stage liquid phase organic crystal growth via liquid cell electron microscopy. *Nanoscale* **2020,** *12* (7), 4636-4644.
(27) Woehl, T. J.; Abellan, P. Defining the radiation chemistry during liquid cell electron microscopy to enable visualization of nanomaterial growth and degradation dynamics. *Journal of microscopy* **2017,** *265* (2), 135-147, DOI: 10.1111/jmi.12508.
(28) Woehl, T. J.; Moser, T.; Evans, J. E.; Ross, F. M. Electron-beam-driven chemical processes during liquid phase transmission electron microscopy. *MRS Bulletin* **2020,** *45* (9), 746-753.
(29) Schneider, N. M.; Norton, M. M.; Mendel, B. J.; Grogan, J. M.; Ross, F. M.; Bau, H. H. Electron–water interactions and implications for liquid cell electron microscopy. *The Journal of Physical Chemistry C* **2014,** *118* (38), 22373-22382.
(30) Park, J. H.; Schneider, N. M.; Grogan, J. M.; Reuter, M. C.; Bau, H. H.; Kodambaka, S.; Ross, F. M. Control of electron beam-induced Au nanocrystal growth kinetics through solution chemistry. *Nano letters* **2015,** *15* (8), 5314-5320.
(31) Francis, S.; Varshney, L.; Tirumalesh, K. Studies on radiation synthesis of polyethyleneimine/acrylamide hydrogels. *Radiation Physics and Chemistry* **2006,** *75* (7), 747-754.
(32) Garrison, W. M. Reaction mechanisms in the radiolysis of peptides, polypeptides, and proteins. *Chemical reviews* **1987,** *87* (2), 381-398.
(33) Shadyro, O.; Sosnovskaya, A.; Vrublevskaya, O. CN bond cleavage reactions on the radiolysis of amino-containing organic compounds and their derivatives in aqueous solutions. *International journal of radiation biology* **2003,** *79* (4), 269-279.
(34) Roder, M.; Wojnarovits, L.; Földiák, G. Pulse radiolysis of aqueous solutions of aromatic hydrocarbons in the presence of oxygen. *International Journal of Radiation Applications and Instrumentation. Part C. Radiation Physics and Chemistry* **1990,** *36* (2), 175-176.
(35) Delaire, J.; Bazouin, J. Primary mechanisms in the radiolysis of amines: pulse and γ-radiolysis of neutral and acidic ethylamine, n-propylamine and ethylenediamine. *Canadian Journal of Chemistry* **1979,** *57* (15), 2013-2021.
(36) Neta, P.; Simic, M.; Hayon, E. Pulse radiolysis of aliphatic acids in aqueous solutions. I. Simple monocarboxylic acids. *The Journal of Physical Chemistry* **1969,** *73* (12), 4207-4213.
(37) Ulanski, P.; Bothe, E.; Hildenbrand, K.; Rosiak, J. M.; von Sonntag, C. Radiolysis of poly (acrylic acid) in aqueous solution. *Radiation Physics and Chemistry* **1995,** *46* (4-6), 909-912.
(38) Ulański, P.; Janik, I.; Rosiak, J. Radiation formation of polymeric nanogels. *Radiation Physics and Chemistry* **1998,** *52* (1-6), 289-294.
(39) Ulański, P.; Kadłubowski, S.; Rosiak, J. M. Synthesis of poly (acrylic acid) nanogels by preparative pulse radiolysis. *Radiation Physics and Chemistry* **2002,** *63* (3-6), 533-537.
(40) Ulanski, P.; Rosiak, J.; Zainuddin, A. Pulse radiolysis of poly (ethylene oxide) in aqueous solution. II. Decay of macroradicals. *Radiation Physics and Chemistry (1993)* **1995,** *46* (4-6), 917-920.
(41) Hauwiller, M. R.; Ondry, J. C.; Chan, C. M.; Khandekar, P.; Yu, J.; Alivisatos, A. P. Gold Nanocrystal Etching as a Means of Probing the Dynamic Chemical Environment in Graphene Liquid Cell Electron Microscopy. *Journal of the American Chemical Society* **2019,** *141* (10), 4428-4437, DOI: 10.1021/jacs.9b00082.
(42) Weiner, R. G.; Chen, D. P.; Unocic, R. R.; Skrabalak, S. E. Impact of Membrane-Induced Particle Immobilization on Seeded Growth Monitored by In Situ Liquid Scanning Transmission Electron Microscopy. *Small* **2016,** *12* (20), 2701-6, DOI: 10.1002/smll.201502974.
(43) Woehl, T. J.; Evans, J. E.; Arslan, I.; Ristenpart, W. D.; Browning, N. D. Direct in situ determination of the mechanisms controlling nanoparticle nucleation and growth. *ACS nano* **2012,** *6* (10), 8599-610, DOI: 10.1021/nn303371y.

(44) Wu, J.; Gao, W.; Yang, H.; Zuo, J. M. Dissolution Kinetics of Oxidative Etching of Cubic and Icosahedral Platinum Nanoparticles Revealed by in Situ Liquid Transmission Electron Microscopy. *ACS nano* **2017,** *11* (2), 1696-1703, DOI: 10.1021/acsnano.6b07541.
(45) Ye, X.; Jones, M. R.; Frechette, L. B.; Chen, Q.; Powers, A. S.; Ercius, P.; Dunn, G.; Rotskoff, G. M.; Nguyen, S. C.; Adiga, V. P.; Zettl, A.; Rabani, E.; Geissler, P. L.; Alivisatos, A. P. Single-particle mapping of nonequilibrium nanocrystal transformations. *Science* **2016,** *354* (6314), 874-877, DOI: 10.1126/science.aah4434.
(46) Zečević, J.; Hermannsdörfer, J.; Schuh, T.; de Jong, K. P.; de Jonge, N. Anisotropic shape changes of silica nanoparticles induced in liquid with scanning transmission electron microscopy. *Small* **2017,** *13* (1), 1602466.
(47) Patterson, J. P.; Abellan, P.; Denny, M. S., Jr.; Park, C.; Browning, N. D.; Cohen, S. M.; Evans, J. E.; Gianneschi, N. C. Observing the growth of metal-organic frameworks by in situ liquid cell transmission electron microscopy. *Journal of the American Chemical Society* **2015,** *137* (23), 7322-8, DOI: 10.1021/jacs.5b00817.
(48) Elgrabli, D.; Dachraoui, W.; Menard-Moyon, C.; Liu, X. J.; Begin, D.; Begin-Colin, S.; Bianco, A.; Gazeau, F.; Alloyeau, D. Carbon Nanotube Degradation in Macrophages: Live Nanoscale Monitoring and Understanding of Biological Pathway. *ACS nano* **2015,** *9* (10), 10113-24, DOI: 10.1021/acsnano.5b03708.
(49) Woehl, T. J.; Kashyap, S.; Firlar, E.; Perez-Gonzalez, T.; Faivre, D.; Trubitsyn, D.; Bazylinski, D. A.; Prozorov, T. Correlative electron and fluorescence microscopy of magnetotactic bacteria in liquid: Toward in Vivo imaging. *Microscopy and Microanalysis* **2015,** *21* (S3), 1499-1500.
(50) Korpanty, J.; Parent, L. R.; Gianneschi, N. C. Enhancing and Mitigating Radiolytic Damage to Soft Matter in Aqueous Phase Liquid-Cell Transmission Electron Microscopy in the Presence of Gold Nanoparticle Sensitizers or Isopropanol Scavengers. *Nano letters* **2021,** *21* (2), 1141-1149.
(51) Schneider, C. A.; Rasband, W. S.; Eliceiri, K. W. NIH Image to ImageJ: 25 years of image analysis. *Nature methods* **2012,** *9* (7), 671-675.
(52) Keskin, S.; de Jonge, N. Reduced radiation damage in transmission electron microscopy of proteins in graphene liquid cells. *Nano letters* **2018,** *18* (12), 7435-7440.
(53) Touve, M. A.; Figg, C. A.; Wright, D. B.; Park, C.; Cantlon, J.; Sumerlin, B. S.; Gianneschi, N. C. Polymerization-induced self-assembly of micelles observed by liquid cell transmission electron microscopy. *ACS central science* **2018,** *4* (5), 543-547.
(54) Wu, H.; Friedrich, H.; Patterson, J. P.; Sommerdijk, N. A.; de Jonge, N. Liquid-Phase Electron Microscopy for Soft Matter Science and Biology. *Advanced materials* **2020**, 2001582.
(55) Woehl, T. J.; Kashyap, S.; Firlar, E.; Perez-Gonzalez, T.; Faivre, D.; Trubitsyn, D.; Bazylinski, D. A.; Prozorov, T. Correlative Electron and Fluorescence Microscopy of Magnetotactic Bacteria in Liquid: Toward In Vivo Imaging. *Scientific Reports* **2014,** *4*, 6854, DOI: 10.1038/srep06854

https://www.nature.com/articles/srep06854#supplementary-information.
(56) Wang, M.; Park, C.; Woehl, T. J. Quantifying the nucleation and growth kinetics of electron beam nanochemistry with liquid cell scanning transmission electron microscopy. *Chemistry of Materials* **2018,** *30* (21), 7727-7736.
(57) Wang, M.; Leff, A. C.; Li, Y.; Woehl, T. J. Visualizing Ligand-Mediated Bimetallic Nanocrystal Formation Pathways with in Situ Liquid-Phase Transmission Electron Microscopy Synthesis. *ACS nano* **2021,** *15* (2), 2578-2588.
(58) Cho, H.; Jones, M. R.; Nguyen, S. C.; Hauwiller, M. R.; Zettl, A.; Alivisatos, A. P. The use of graphene and its derivatives for liquid-phase transmission electron microscopy of radiation-sensitive specimens. *Nano letters* **2017,** *17* (1), 414-420.
(59) Wang, H.; Nagamanasa, K. H.; Kim, Y.-J.; Kwon, O.-H.; Granick, S. Longer-lasting electron-based microscopy of single molecules in aqueous medium. *ACS nano* **2018,** *12* (8), 8572-8578.
(60) Chapiro, A. Radiation induced polymerization. *Radiation Physics and Chemistry (1977)* **1979,** *14* (1-2), 101-116.
(61) Matusiak, M.; Kadlubowski, S.; Rosiak, J. M. Nanogels synthesized by radiation-induced intramolecular crosslinking of water-soluble polymers. *Radiation Physics and Chemistry* **2020,** *169*, 108099.

(62) Cleland, M.; Parks, L.; Cheng, S. Applications for radiation processing of materials. *Nuclear Instruments and Methods in Physics Research Section B: Beam Interactions with Materials and Atoms* **2003,** *208*, 66-73.
(63) Gibson, W.; Patterson, J. P. Liquid Phase Electron Microscopy Provides Opportunities in Polymer Synthesis and Manufacturing. *Macromolecules* **2021**.
(64) Woehl, T. J.; Prozorov, T. The mechanisms for nanoparticle surface diffusion and chain self-assembly determined from real-time nanoscale kinetics in liquid. *The Journal of Physical Chemistry C* **2015,** *119* (36), 21261-21269.
(65) Jiang, N. Note on in situ (scanning) transmission electron microscopy study of liquid samples. *Ultramicroscopy* **2017,** *179*, 81-83.
(66) Yesibolati, M. N.; Mortensen, K. I.; Sun, H.; Brostrøm, A.; Tidemand-Lichtenberg, S.; Mølhave, K. Unhindered brownian motion of individual nanoparticles in liquid-phase scanning transmission electron microscopy. *Nano letters* **2020,** *20* (10), 7108-7115.
(67) Mehdi, B.; Stevens, A.; Kovarik, L.; Jiang, N.; Mehta, H.; Liyu, A.; Reehl, S.; Stanfill, B.; Luzi, L.; Hao, W. Controlling the spatio-temporal dose distribution during STEM imaging by subsampled acquisition: In-situ observations of kinetic processes in liquids. *Applied Physics Letters* **2019,** *115* (6), 063102.
(68) Gupta, T.; Schneider, N. M.; Park, J. H.; Steingart, D.; Ross, F. M. Spatially dependent dose rate in liquid cell transmission electron microscopy. *Nanoscale* **2018,** *10* (16), 7702-7710, DOI: 10.1039/c8nr01935e.
(69) Verch, A.; Pfaff, M.; de Jonge, N. Exceptionally Slow Movement of Gold Nanoparticles at a Solid/Liquid Interface Investigated by Scanning Transmission Electron Microscopy. *Langmuir : the ACS journal of surfaces and colloids* **2015,** *31* (25), 6956-64, DOI: 10.1021/acs.langmuir.5b00150.
(70) Chee, S. W.; Baraissov, Z.; Loh, N. D.; Matsudaira, P. T.; Mirsaidov, U. Desorption-mediated motion of nanoparticles at the liquid–solid interface. *The Journal of Physical Chemistry C* **2016,** *120* (36), 20462-20470.
(71) Ulanski, P.; Bothe, E.; Hildenbrand, K.; von Sonntag, C. Free-Radical-Induced Chain Breakage and Depolymerization of Poly (methacrylic acid): Equilibrium Polymerization in Aqueous Solution at Room Temperature. *Chemistry–A European Journal* **2000,** *6* (21), 3922-3934.
(72) Ulanski, P.; von Sonntag, C. OH-Radical-induced chain scission of chitosan in the absence and presence of dioxygen. *Journal of the Chemical Society, Perkin Transactions 2* **2000,** (10), 2022-2028.
(73) Gröllmann, U.; Schnabel, W. On the kinetics of polymer degradation in solution, 9. Pulse radiolysis of poly (ethylene oxide). *Die Makromolekulare Chemie: Macromolecular Chemistry and Physics* **1980,** *181* (6), 1215-1226.
(74) Gröllmann, U.; Schnabel, W. Free radical-induced oxidative degradation of polyacrylamide in aqueous solution. *Polymer Degradation and Stability* **1982,** *4* (3), 203-212.

Figures

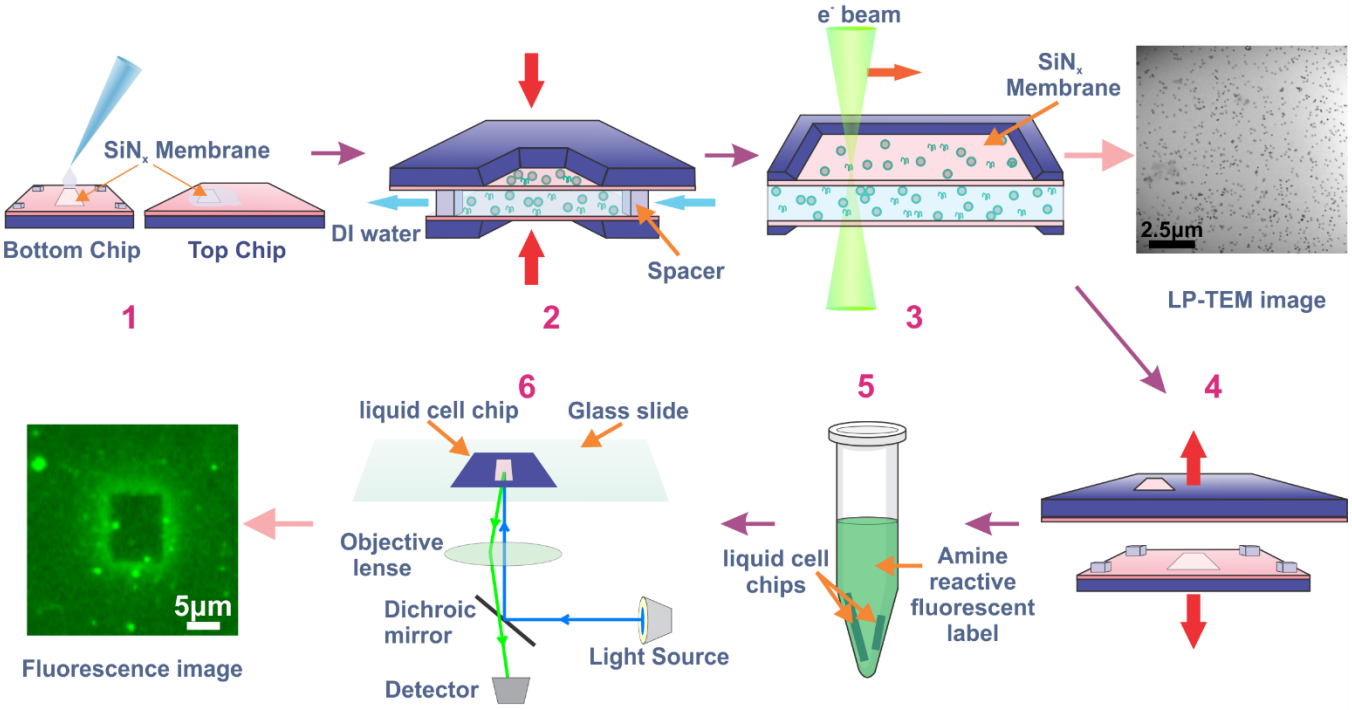

Figure 1. Summary of the method for correlative LP-TEM and FM visualization of capping ligand damage. (1) Silver nanoparticles were drop cast and dried onto cleaned silicon nitride membranes, which were (2) assembled in the liquid cell. (3) Various regions of the sample were imaged in the TEM under different conditions. (4) The sample was disassembled after removing from the TEM and (5) the BPEI ligands were fluorescently labeled by incubating with amine reactive fluorescent molecules. (6) The chips were imaged with FM to visualize electron beam induced reactions with BPEI ligands.

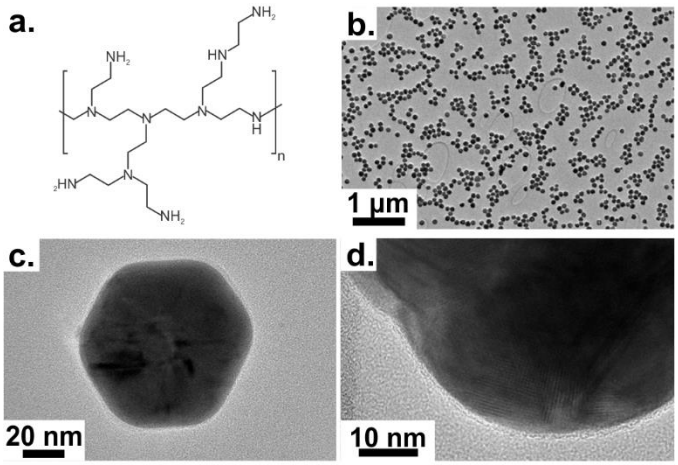

Figure 2. Branched polyethylenemine (BPEI) and TEM images of silver nanoparticles in the dry state. (a) Molecular structure of BPEI. (b) Low magnification TEM image of BPEI coated silver nanoparticles. (c) HRTEM image of a single nanoparticle showing the particle shape. (d) HRTEM image showing the BPEI ligand layer on a polycrystalline silver nanoparticle.

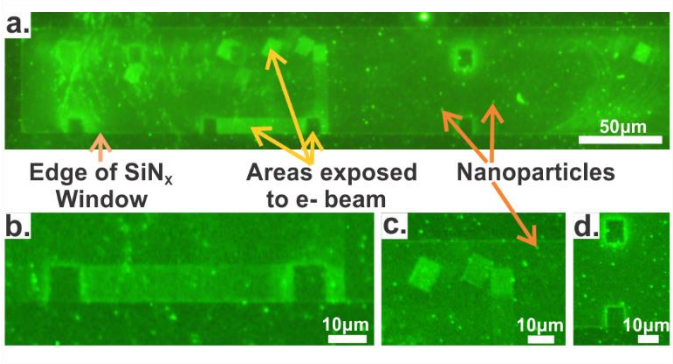

Figure 3. Exemplary FM images of a fluorescent labeled silicon nitride membrane after a LP-TEM experiment. The green fluorescence intensity shows the relative local thickness of BPEI ligand. (a) Survey image of the silicon nitride membrane showing various fluorescent features created by presence of nanoparticles and electron beam exposure. (b) Sample translation during LP-TEM with continuous imaging created pathways of bright fluorescence intensity due to brief (seconds) electron beam exposure. (c) STEM scan rotation can be observed by a change in the angle of the bright fluorescent square image regions. (d) Different exposure times and cumulative doses created image regions with different fluorescence intensity compared to the background.

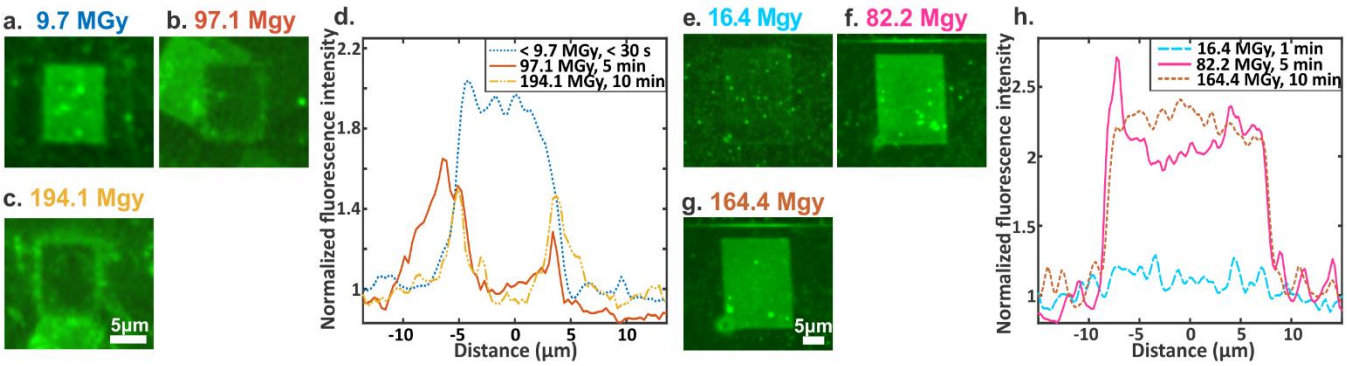

Figure 4. Effect of cumulative dose on the fluorescence intensity of the silicon nitride membrane with (a) – (c) and without (e) – (g) silver nanoparticles deposited on the membrane. (a) – (c) FM images of irradiated sample regions with BPEI coated nanoparticles irradiated at a dose rate of 0.324 MGy/s for times of (a) < 30 s, (b) 5 minutes, and (c) 10 minutes. (d) Fluorescence intensity measured along a horizontal line drawn across the center of each irradiation region in (a) – (c). (e) – (g) FM images of irradiated sample regions with only BPEI ligands irradiated at a dose rate of 0.274 MGy/s for times of (e) 1 minute, (f) 5 minutes, and (g) 10 minutes. (h) Fluorescence intensity measured along a horizontal line drawn across the center of each irradiation region in (e) – (g). The fluorescence intensity of each irradiated region was normalized to the local background intensity.

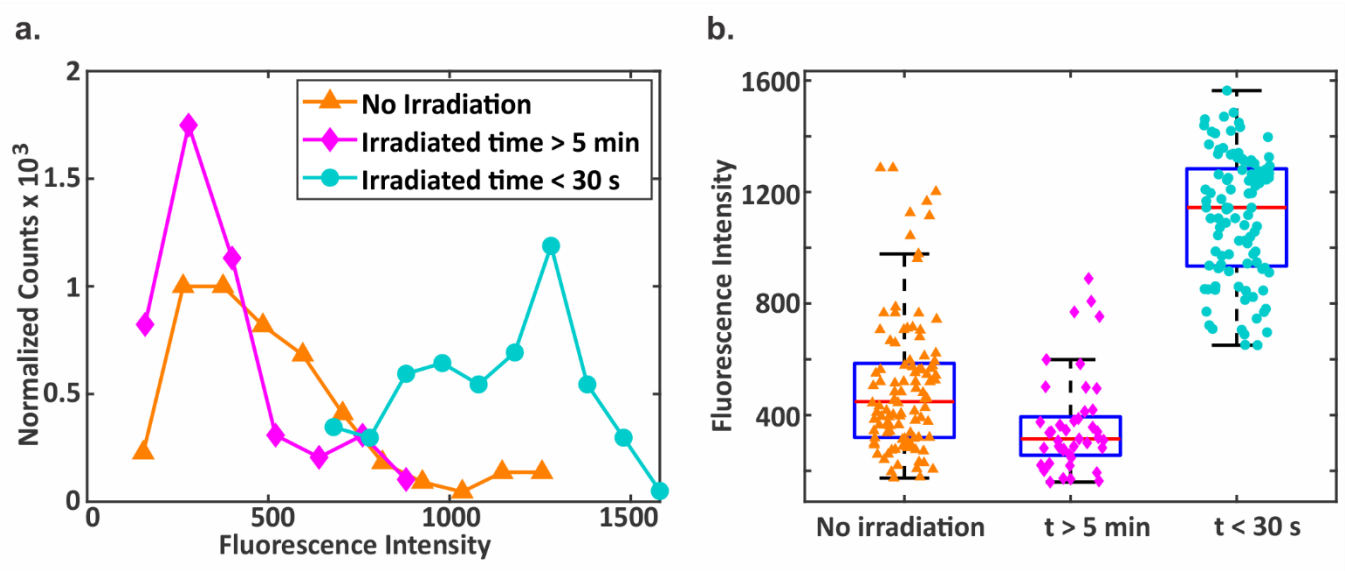

Figure 5. Fluorescence intensity distributions of silver nanoparticles after electron beam exposure in DI water. Intensity data were measured from the sample regions shown in **Figure 3**. (a) Probability distribution functions of silver nanoparticle fluorescence intensities for particles that were not irradiated (orange triangles), irradiated for < 30 s (< 9.7 MGy, cyan circles), and irradiated for > 5 minutes (> 97.1 MGy, pink diamonds). (b) Box plots of nanoparticle fluorescence intensities for each condition. Wilcoxon rank-sum tests showed there were statistically significant differences between each fluorescence intensity distribution ($P < 0.005$). Fluorescence intensities of 104, 45, and 105 particles were measured from the regions of no irradiation, irradiation for > 5 minutes, and irradiation for < 30 seconds, respectively.

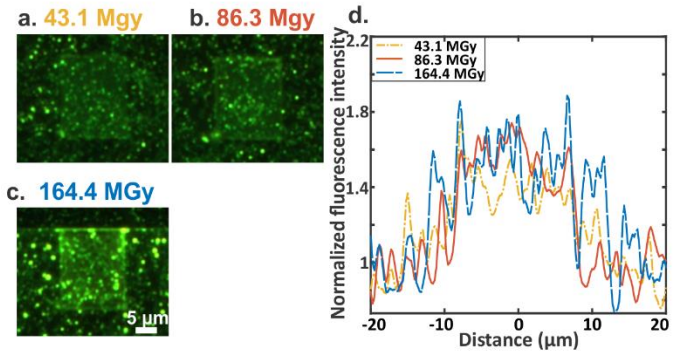

Figure 6. The fluorescence intensity of irradiated silicon nitride regions for a nanoparticle sample containing 1 M tert-butanol. (a) – (c) FM images corresponding to image areas irradiated at a dose rate of 0.144 MGy/s for times of (a) 5 minutes and (b) 10 minutes and irradiated at a dose rate of 0.274 MGy/s for (c) 10 minutes. (d) Fluorescence intensity measured along a horizontal line drawn across each irradiated region in (a) – (c).

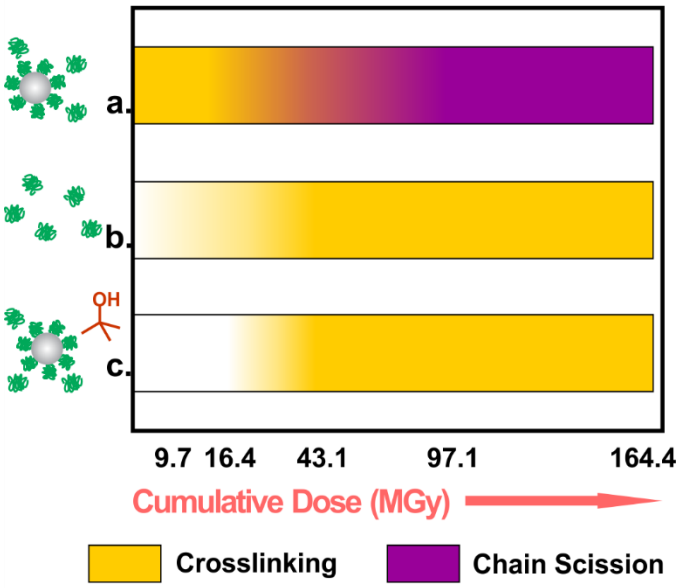

Figure 7. Qualitative schematic showing the prevalence of crosslinking and chain scission reactions in BPEI ligands as a function of cumulative dose as determined by FM for (a) a sample with nanoparticles and excess BPEI ligands in DI water, (b) a sample with only excess BPEI ligands in DI water and (c) a sample with nanoparticles and excess BPEI ligands in 1 M aqueous tert-butanol. In sample (a) the exact crossover point from crosslinking to chain scission was unknown but occurred between 16.4 – 43.1 MGy. In both (b) and (c) the regions with lighter color represent cumulative doses where little to no change in the irradiated area was observed by FM. The x-axis is not to scale.

Table of contents figure.